Impact of surface and laser-induced noise on the spectral stability of implanted nitrogen-vacancy centers in diamond

Srivatsa Chakravarthi [1], Christian Pederson,[2] Zeeshawn Kazi [2], Andrew Ivanov,[2] and Kai-Mei C. Fu[1,2]

[1]*Electrical and Computer Engineering Department, University of Washington, Seattle, Washington 98105, USA*
[2]*Physics Department, University of Washington, Seattle, Washington 98105, USA*

Scalable realizations of quantum network technologies utilizing the nitrogen-vacancy (NV) center in diamond require creation of optically coherent NV centers in close proximity to a surface for coupling to optical structures. We create single NV centers by ^{15}N ion implantation and high-temperature vacuum annealing. The origin of the NV centers is established by optically detected magnetic resonance spectroscopy for nitrogen isotope identification. Near-lifetime-limited optical linewidths (<60 MHz) are observed for the majority of the normal-implant ($7°$, $\approx$100 nm deep) ^{15}NV centers. Long-term stability of the NV$^-$ charge state and emission frequency is demonstrated. The effect of NV-surface interaction is investigated by varying the implantation angle for a fixed ion energy, and thus lattice damage profile. In contrast to the normal-implant condition, NVs from an oblique implant ($85°$, $\approx$20 nm deep) exhibit substantially reduced optical coherence. Our results imply that the surface is a larger source of perturbation than implantation damage for shallow implanted NVs. This work supports the viability of ion implantation for formation of optically stable NV centers. However, careful surface preparation will be necessary for scalable defect engineering.

I. INTRODUCTION

Nitrogen-vacancy (NV) point defects in diamond combine optical addressability [1–3] with long spin coherence times [4], making them promising candidates for quantum networking [5,6]. NV centers in diamond have been used to demonstrate essential ingredients for quantum networks in recent experiments, including on-demand remote entanglement generation [7,8], coherent control of multiple nearby nuclear spin memories [9], and memory-enhanced quantum communication [8,10]. For networking schemes, optical coherence and photon collection efficiency are key figures of merit. Nanophotonic integration of NV centers has demonstrated potential for high collection efficiency and scalable integration [11–14] and thus should enable the scaling of quantum entanglement networks. The small mode volume needed for significant photonic coupling requires localization of NV centers to within tens of nanometers from diamond surfaces. Hybrid materials platforms [13,15], which minimize diamond fabrication, utilize evanescent coupling, requiring the NV centers to be in even closer surface proximity. Nitrogen ion (N$^+$) implantation followed by high-temperature annealing is a commonly utilized process for targeted spatial localization of NV centers for device integration. However, recent published results by van Dam *et al.* [16] and Kasperczyk *et al.* [17] determined that centers with high optical coherence created by N$^+$ implantation and annealing are predominantly formed by implantation-induced vacancies diffusing and combining with native nitrogen. As vacancies are relatively mobile at annealing temperatures [18–21], this result implies loss of localization and precludes deterministic photonic device integration.

The optical coherence of shallow NV centers can suffer degradation from two sources: (1) charge traps formed in the bulk from the implantation and annealing process and (2) charge traps associated with the surface or subsurface of diamond. Ionization of charge traps produces a dynamically changing electric field which couples to the different dipole moments of the ground and excited states of the NV centers [15,22–24]. This effect manifests as linewidth broadening and spectral diffusion of the NV optical transitions. Since the prescription for each possible source is quite different, it is important to identify the relevant culprit. Here, we show that for $\approx$100 nm implant depth, it is possible to create ^{15}NV centers with typical optical transition linewidths <60 MHz. Additionally, the long-term spectral stability of the NV transitions to within 200 MHz is demonstrated. For this implant condition, given the average NV-surface distance, we expect bulk sources to dominate optical decoherence. The observed spectral stability implies that bulk sources can be overcome.

Encouraged by the 100 nm implantation results, we explore the possibility of implanting coherent centers closer to the surface. Shallower centers allow for enhanced optical coupling [13] for hybrid materials devices. We create NV centers at $\approx$20 nm by changing the angle of implantation as opposed to varying the energy of implantation. Hence the local damage profile around an NV center is similar to the 100 nm implantation condition, merely rotated relative to the surface. Here, we find that the optical linewidths are orders of magnitude larger and are accompanied by decreased spectral stability.

Combined, these observations strongly imply that the proximity to the diamond surface is the dominant source of optical decoherence and that the bulk implantation damage

profile is not the limiting factor for shallow implanted NV centers.

II. EXPERIMENT

A. Samples

In our primary study, to elucidate the effect of the surface on the optical properties of implanted NV centers, we utilize two identical chemical vapor deposition diamond samples, samples A and B (Element Six, electronic grade, N < 1 ppb, B < 1 ppb), with $\langle 100 \rangle$ surfaces. As purchased, the diamond surfaces are polished to less than 1 nm RMS surface roughness. Both samples are processed identically unless stated otherwise. First, we etch away ≈ 5 μm from the surface using plasma reactive-ion etching to remove polishing damage [23]. We take the following precautions to avoid the micromasking that is a common occurrence during diamond etching: At each step the diamonds are cleaned in a boiling 1 : 1 : 1 mixture of H_2SO_4, H_2NO_3, and $HClO_4$ at 260 °C for 1 h to remove organic contaminants and graphitic carbon [23]. A sapphire carrier wafer is utilized to prevent silicon contamination of the diamond surface during the etch [25]. We utilize a two-step Ar/Cl plasma (physical etching via sputtering) followed by O_2 plasma (chemical etching via oxidation) process to remove any deposited material that may result in micromasking (process details are provided in Appendix A). The total etch duration is 45 min of Ar/Cl_2 etching and 20 min of O_2 etching. After processing, both diamonds have nearly identical surface morphology with sample A (B) exhibiting 0.63 (0.43) nm RMS roughness [Fig. 1(a)].

We implant both sample A and sample B with ^{15}N at identical energies and effective beam dosages of 85 keV and 3×10^9 ions/cm^2. The implantation angles for samples A and B are 7° and 85°, respectively. We model the effect of the different ion incidence angles on the implantation profile using the Stopping and Range of Ions in Matter (SRIM) code [26]. For sample A (B), the average depth of the ^{15}N atoms is 100 ± 20 (21 ± 13) nm below the surface. Although the effective beam dosage is identical for the two samples, approximately 40% of the incident ions are backscattered for sample B. This backscattering is a geometric consequence of rotating the damage profile relative to the surface, such that some of the scattered ions escape the diamond surface. Hence the final ^{15}N density in sample B is predicted to have 60% of the density of sample A.

The samples are vacuum annealed at $<1.4 \times 10^{-7}$ mbar and 1100 °C for 2 h with long ramp times as described in Refs. [16,23]. This is followed by a short 2 h anneal at 435 °C under O_2 flow to oxygen-terminate the surface and stabilize the negative charge state [27,28] of the near-surface NV centers.

In addition, we characterize four supplemental diamond NV implantation samples (samples C–F) to support the reproducibility of the primary study. These diamond substrates have identical specifications (Element Six, electronic grade) but are sourced from different growth runs. Preimplantation, all samples are processed as detailed in this section. (The specifics of implantation and annealing conditions for each sample are provided in the table in Fig. 4.)
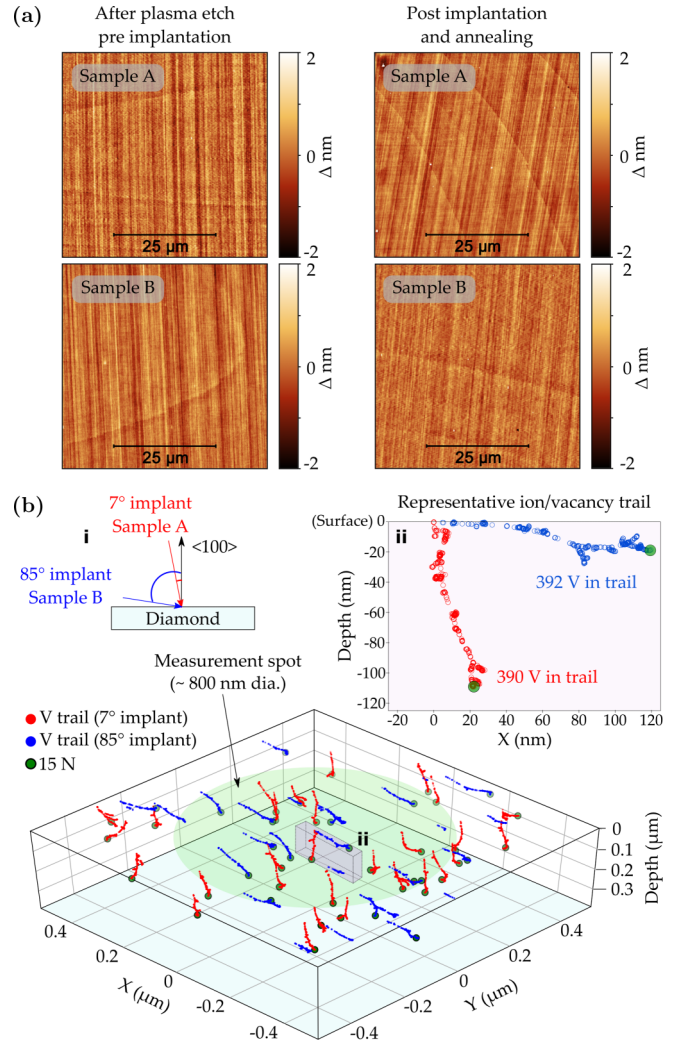

FIG. 1. Diamond surface preparation and simulations of implantation conditions: (a) Morphology of the diamond surface measured by atomic force microscopy. The RMS surface roughness for sample A (B) was measured to be 0.63 (0.43) nm before implantation and 0.56 (0.30) nm after implantation and annealing. (b) A simulation of the implantation profile obtained by SRIM for sample A (red, 7°) and sample B (blue, 85°) showing the damage trails and final positions of implanted ^{15}N atoms. The green circle represents our excitation laser spot. Note that the implantation yield is low (<5%); hence within an excitation spot there is a small probability that each trail results in a NV center upon annealing. Inset i: Illustration of the implantation geometry. Inset ii: A cross section of the simulation showing the ion damage trails for the two implant angles. The total number of vacancies generated per ion is similar for both the implant angles. However, on sample B, some ^{15}N atoms are lost due to ion scatter out of the surface. Here, dia., diameter; V, vacancy.

B. Measurements

A confocal microscope comprising a 532-nm diode-pumped solid-state (DPSS) laser and ×60 [numerical aperture (NA) = 0.7] objective lens is used to scan over 80×80 μm^2 areas using a piezo stage. A polarizing beamsplitter with an automated half-wave plate is used in the excitation path to preferentially excite a given NV orientation.
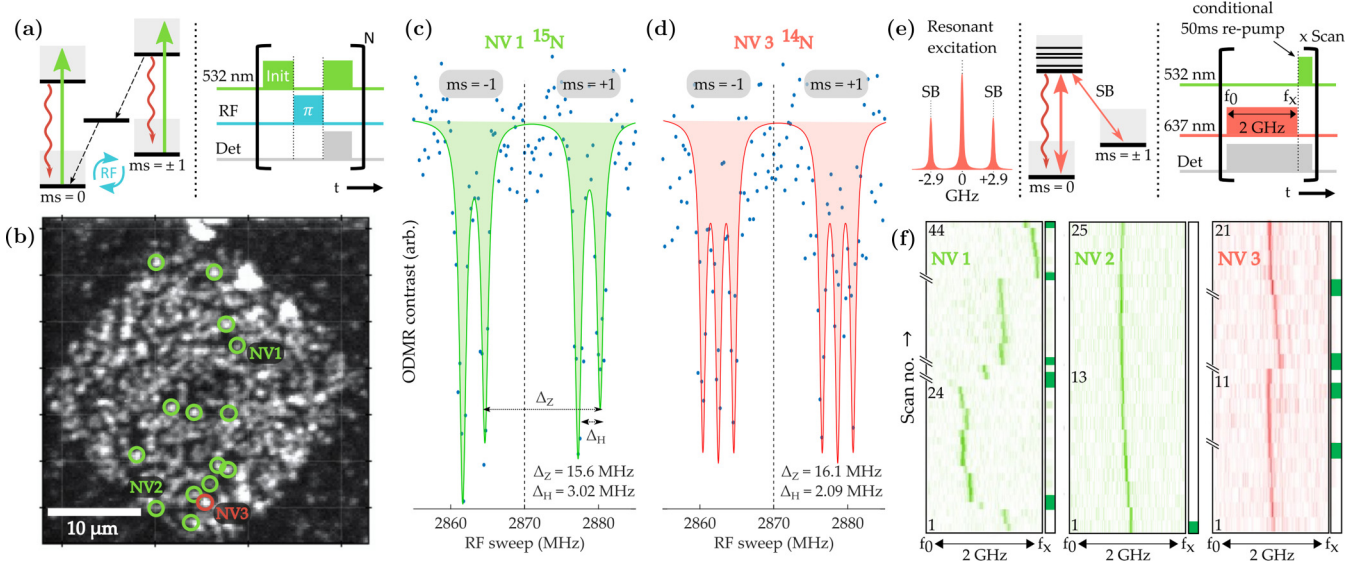
FIG. 2. Correlated NV ODMR (RT) and PLE (T < 12 K) measurements on sample A. (a) Pulsed ODMR scheme utilized to identify the N isotope. Laser and radio-frequency (RF) pulses are generated by an acousto-optical modulator and RF switch, respectively (laser power, 0.8–1.0 mW; spot diameter, ~800 nm). Pulses and photon collection are triggered by a programmable pulse generator. Det, detection; Init, Initialization pulse. (b) Confocal PL map of the implanted region with the measured NV centers indicated by their isotope (green, ^{15}N; red, ^{14}N). (c) ODMR spectra for the marked NV incorporating implanted ^{15}N. (d) ODMR spectra for the marked NV incorporating grown-in ^{14}N. (e) Resonant excitation (PLE) scheme utilized for characterizing the optical coherence of the marked NV centers. Sidebands (SBs) at 2.9 GHz are added (using an electro-optic modulator) to the scanning resonant laser to counteract optical spin pumping. Upon detection of an NV$^-$ to NV^0 ionization event (indicated by lack of NV$^-$ PL) a 50 ms off-resonant green repump is used to reset the NV charge state. (f) Time traces of PLE scans measured at 10.5 K for three NV centers. Off-resonant repumps between scans are indicated by green squares along the right column; this induces large spectral jumps in many ^{15}NV centers (e.g., NV 1). The "\\" markers along the scan axis indicate discarded scans where no NV PL is observed. The PLE traces for ^{15}NV centers typically show long periods of spectral stability between repump pulses.

To identify the nitrogen isotope associated with each NV center, we use optically detected magnetic resonance (ODMR) spectroscopy. For an NV in the spin quantum number $m_s = \pm 1$ ground spin sublevel, reduced photoluminescence (PL) is observed upon off-resonant excitation due a small likelihood ($\approx 20\%$) of relaxation through the dark intersystem crossing transition [29,30] [dashed arrows, Fig. 2(a)]. The samples are placed in a weak magnetic field (≈ 5 G) that splits the $m_s = \pm 1$ ground spin sublevels. Radio-frequency (RF) excitation is delivered via a small copper loop (radius 0.3 mm) suspended ≈ 50 μm above the diamond sample. A short (5 μs) off-resonant 532-nm laser pulse initializes the NV into the $m_s = 0$ spin state. Next, an RF π-pulse (0.8 μs) rotates the NV spin state before time-resolved NV PL is recorded during the subsequent short (5 μs) readout laser pulse. The π-pulse area is initially calibrated by performing a Rabi experiment. The pulse sequence is repeated while sweeping the RF driving frequency over all the NV ground-state spin transitions. The resulting two-dip (three-dip) PL intensity spectrum corresponds to the ^{15}N (^{14}N) NV-N ground-state hyperfine interaction [1,31], indicating that the NV incorporates an implanted or grown-in nitrogen atom [Figs. 2(c) and 2(d)]. ODMR spectra are measured at room temperature (RT) for randomly sampled NV centers in the implantation region [Fig. 2(b)] and fit to a three-dip (^{14}NV) or two-dip (^{15}NV) Lorentzian. The positions of the sampled NV centers are recorded. The samples are then cooled to <12 K in a closed-cycle cryostat for spectral characterization of the selected NV centers.

Low-temperature NV$^-$ PL spectra under cw 532-nm excitation provide the inhomogeneous distribution of the zero-phonon line (ZPL) transition (Fig. 5) arising from variations in the local strain and electric field environment of individual centers. The NV charge state ratio (NV$^-$/NV^0) is also recorded as a function of the excitation intensity for a subset of centers (Appendix C). Additionally, high-resolution photo-luminescence excitation (PLE) spectroscopy provides insight into the optical coherence and temporal spectral stability of individual NV centers. In PLE measurements, a narrow-band tunable laser is scanned across the NV$^-$ ZPL while collecting the NV$^-$ phonon-sideband PL (650–800 nm) [Fig. 2(e)]. The resonant laser and accompanying 2.9-GHz sidebands simultaneously drive the $\{m_s = 0, m_s = \pm 1\} \rightarrow \{E_x, E_y\}$ transitions [32–34].

From the PLE spectra we collect statistics on the ZPL single-scan linewidth as well as the scan-to-scan variation in the ZPL frequency. During PLE we can sometimes observe a loss of the NV$^-$ PL signal due to ionization to the NV^0 state; to reinitialize into the NV$^-$ charge state, we apply a short low-power 532-nm repump pulse (50 ms) between scans [as indicated by the green markers in Fig. 2(f)]. The interval between repump pulses is an additional indicator of the stability of the NV$^-$ charge state.

III. CORRELATED ODMR AND PLE SPECTROSCOPY

On sample A, ODMR was performed on 32 NV centers with 26 centers identified as ^{15}NV and 1 as ^{14}NV; the

remaining 5 NVs could not be conclusively identified. Similarly, on sample B, ODMR was performed on 38 NV centers with 27 centers identified as ^{15}NV and 2 as ^{14}NV; the remaining 9 NVs could not be identified. The observed total NV density for sample A (B) is 1.2 per μm^2 (0.3 per μm^2), which corresponds to an implantation conversion yield of 4% (1%). For both these samples, no grown-in NVs were observed in an 80×80 μm^2 area at a depth of 50 μm implying very low native N_s density [35]. Considering the natural abundance of ^{15}N (0.4%) and the ^{15}NV-to-^{14}NV ratio r for both samples (r_A = 26, r_B = 13.5), it is clear that for our diamond substrates and implantation conditions, NV formation incorporating implanted nitrogen is favored.

First let us consider sample A. The single-NV low-temperature ZPL spectra under off-resonant 532-nm excitation are typically spectrometer resolution limited ($\Delta\lambda$ = 0.021 nm). PLE spectroscopy reveals that both ^{15}N and ^{14}N centers typically exhibit near-lifetime-limited linewidths. A sequence of laser scans over a span of $\approx$10 min (each scan is 4–8 s in duration) gives us a median linewidth of <60 MHz for 12 out of 16 centers [Fig. 3(a)]. This linewidth is computed by individually fitting each scan to a Lorentzian. The laser intensity is set between 30 and 60 nW with a scan rate of 1–2.5 GHz/s. A linewidth power dependence measurement was performed on two centers to ensure that the observed linewidths are not significantly power broadened in our intensity range. The PLE results are summarized in Fig. 3(a); the colored boxes mark the fitted linewidths between the first and third quartiles. This interquartile range is an indicator of spectral diffusion ($\Delta\nu$) of the NV ZPL during a single resonant laser scan (on a timescale of milliseconds).

Additionally, by tracking the ZPL frequency between scans, we can characterize the long-term spectral stability (on a timescale of seconds). We calculate this spectral variation ($\Delta\omega$) by recording the change in ZPL frequency between subsequent scans [Fig. 3(b)]. Here, we emphasize that an off-resonant repump pulse is only applied when no NV PL is detected (i.e., NV$^-$ has ionized to NV^0), emulating emerging NV quantum networking protocols [7,8]. The median spectral variation is typically <100 MHz, for long periods (60–300 s) between repumps. We observe that most ^{15}NV centers experience large spectral jumps ($\approx$500 MHz) after an off-resonant repump pulse. These jumps occur in 95% of the repump events. In Fig. 3(b), the blue markers indicate repump-triggered spectral jumps. This is the only metric where we see a clear advantage for the ^{14}NV also observed on sample A (Fig. 3, red). It is unclear at this time whether the repump-triggered perturbation originates at the surface (with the single ^{14}NV lying deeper within the sample) or from local implantation damage. Nevertheless, it may still be mitigated with the use of a low-power resonant NV^0 repump pulse [36].

Sample B reveals a different story: The low-temperature ZPL spectra under off-resonant 532-nm excitation for individual NV centers is much broader (0.02–0.25 nm). Given that the lattice damage profile is similar to sample A, this spectral broadening could be attributed to rapid fluctuations of surface charges effectively Stark-tuning the NV centers within the exposure duration of the spectra. Such rapid ZPL fluctuations make resonant 637-nm PLE measurements very challenging. Of the six NV centers randomly sampled, only

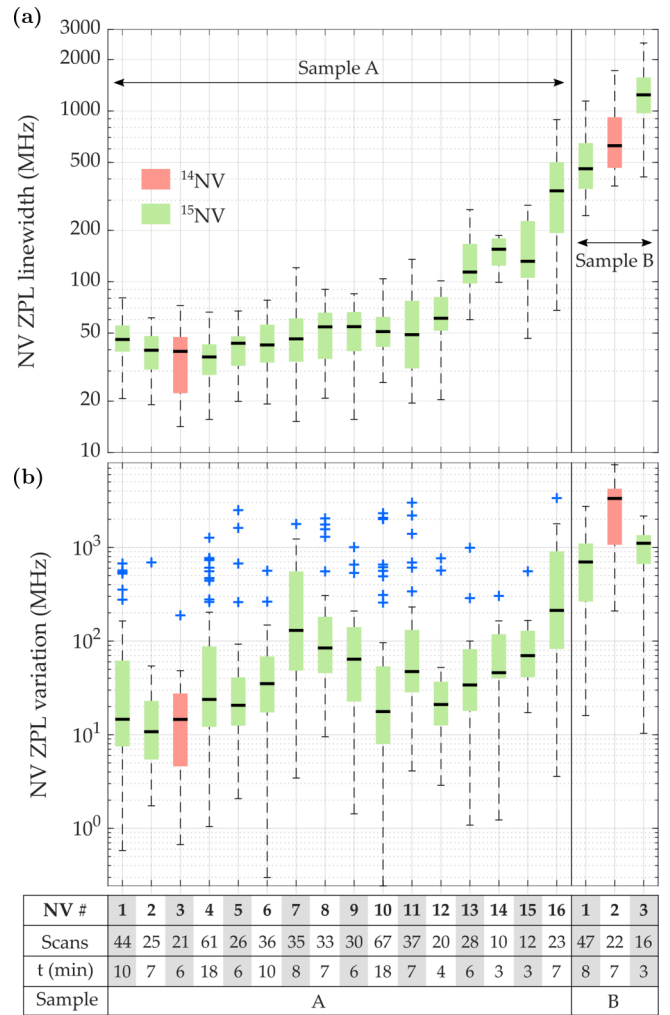| NV #	1	2	3	4	5	6	7	8	9	10	11	12	13	14	15	16	1	2	3
Scans	44	25	21	61	26	36	35	33	30	67	37	20	28	10	12	23	47	22	16
t (min)	10	7	6	18	6	10	8	7	6	18	7	4	6	3	3	7	8	7	3
Sample	A																B		

FIG. 3. Photoluminescence excitation characteristics of measured NV centers on samples A and B. (a) The fitted Lorentzian full width at half maximum (FWHM) distributions for each observed NV. The colored boxes and black markers represent the interquartile range and median linewidth, respectively. The total number of scans and measurement duration comprising each distribution are recorded in the accompanying table. The PLE traces for NV centers 1–3 are also shown in Fig. 2(f). (b) The distributions of the scan-to-scan change in the center frequency of the fits, representing spectral variation. Off-resonant repump pulses are only applied when NV ionization is detected. On average, there are six repump events over a measurement duration of 10 min. The blue markers indicate large spectral jumps after repump pulses.

three showed PLE signal. All three NV centers (two ^{15}N and one ^{14}N) exhibit broad median linewidths (0.5–1.2 GHz) and increased spectral variability (Fig. 3).

Finally, we confirm that the NV$^-$ charge state is preferred across the full range of optical powers (15–600 μW of 532-nm excitation) for both samples A and B (Appendix C).

IV. AUTOMATED SPECTROSCOPY

To corroborate the data from our primary samples (samples A and B), we present automated ODMR, PLE, and low-temperature off-resonant PL spectroscopy data sets on
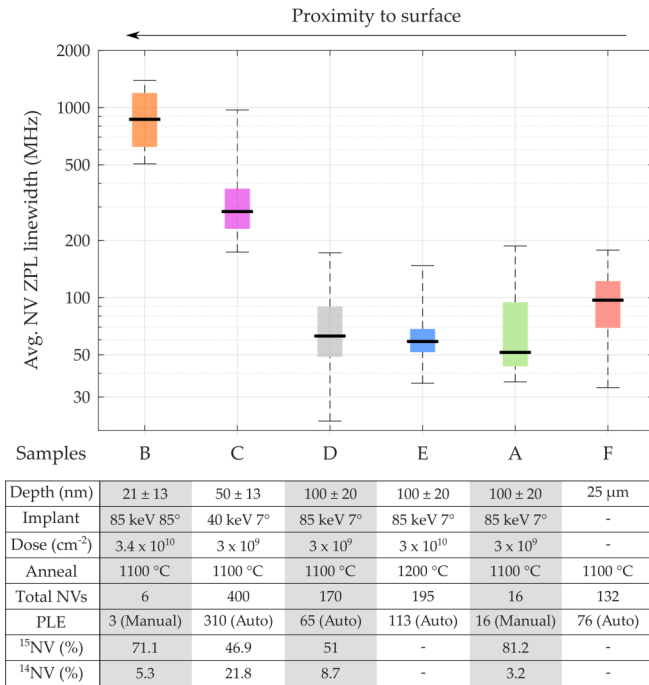
FIG. 4. Automated ODMR and PLE measurements are performed on four additional samples (samples C–F). We are not able to track the NV centers between ODMR and PLE with the automated protocol. The ODMR ^{15}NV-to-^{14}NV ratio suggests predominance of ^{15}NVs across all implanted samples. Similarly to the previous data set (Fig. 3), the average (Avg.) linewidth for each individual NV is computed as the mean FWHM obtained by fitting each of the 30 frequency scans to a Lorentzian. Automated PLE scans performed on deep grown-in NVs (25 μm from surface, sample F) are used as a reference.

four other samples (samples C–F). Our automation procedure allows us to sample hundreds of NV centers; however, we are unable to track individual NV centers between the PL, PLE, and ODMR data sets. Details of the automated measurement protocol are provided in Appendix B.

First, let us consider samples D and E with similar implant conditions (^{15}N, 85 keV, 7°) to sample A. Uncorrelated ODMR measurements on sample D show that most centers are ^{15}N. The measured average ZPL linewidth distribution (Fig. 4) of hundreds of NV centers tracks well with the data set from sample A, indicating the reproducibility of narrow-linewidth ^{15}NV centers. In the ideal case, the linewidth of NV centers created through ion implantation and annealing would be equal to the linewidth observed in background NV centers distributed throughout the sample. No background NV centers could be identified in either sample A or sample B, and a low density prohibited automated measurements in samples C, D, and E. Automated PLE measurements on native NV centers 25 μm within sample F, a similar electronic-grade sample that has undergone high-temperature annealing (with no implantation), serve as our reference. From the data presented in Fig. 4, the average NV linewidth distribution of all the 85 keV, 7° implant samples are in agreement with the reference sample.

Next, we examine the shallow-implantation samples. The average ZPL linewidth distribution in Fig. 4 shows that both
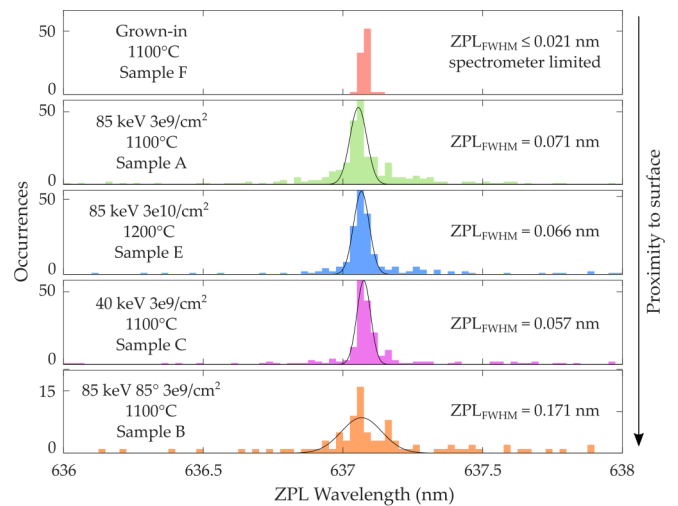

FIG. 5. The NV ZPL inhomogeneous distribution. The histogram is generated by recording the center wavelength of all peaks observed with 532-nm excitation from locations within an implantation region (except the grown-in reference NV centers) on the respective samples. Note that no distinction is made between the different transitions associated with the NV excited state spin sublevels. The bin size is 0.025 nm, and the spectrometer resolution is 0.021 nm. The histogram data are fitted to a Gaussian to extract the FWHM of the distribution. Sample B shows an obvious deviation from other samples.

the shallow-NV samples, sample C (40 keV, 7°) and sample B (85 keV, 85°), exhibit decreased optical coherence. This is despite the fact that initial implantation damage for sample C is significantly lower compared with samples A, D, and E (85 keV, 7°). We can use the average number of vacancies (V) generated per implanted ion trail as an analog for local lattice damage. From SRIM [26] simulations, sample C incorporates 203 V/ion, whereas samples A, B, D, and E incorporate 390 V/ion. This provides further evidence that the broadening seen for the shallow implants is unrelated to the implantation damage at these energies and dosages and instead is a result of charge traps associated with the surface.

In addition, low-temperature PL spectra (off-resonant excitation) from a large number of NV centers provides the inhomogeneous ZPL distribution (Fig. 5). Regardless of the variations in the total implant damage (V/μm^3), the inhomogeneous NV ZPL distributions are similar for samples A, C, and E (Gaussian fit FWHM = 52.5, 42.1, and 48.8 GHz, respectively). The grown-in NV centers exhibit a narrower ZPL spread (FWHM $\leqslant$ 15.4 GHz, spectrometer resolution limited). Finally, the ZPL distribution for sample B is much broader (FWHM = 126 GHz) than any of our other samples. A comparison suggests that there is still a small amount of residual strain remaining in the implantation samples.

V. CONCLUSION

Lattice damage from the ion-implantation process introduces localized perturbations of the defect environment. Our result with the 85 keV, 7° implant samples indicates that much of this damage can be annealed out for an ^{15}NV created

directly from an implanted nitrogen. We observe that ^{15}NV centers exhibit long periods of spectral stability, wherein their spectral characteristics are akin to optically coherent grown-in NV centers. The implanted ^{15}NV and grown-in centers exhibit comparable median optical linewidths. However, we do see distinct advantages for grown-in centers in terms of behavior under off-resonant green repump and inhomogeneous ZPL distribution. For ^{15}NV centers, green repump pulses used to reinitialize the NV charge state introduce large spectral variation ($\approx$500 MHz). This behavior hints at why our ^{15}NV linewidths are qualitatively different from those of van Dam *et al.* [16] and Kasperczyk *et al.* [17]. Those studies utilized repump pulses for every scan, which we can see would cause linewidth broadening into gigahertz frequency. In fact, an analysis considering only the PLE scans immediately after the repump pulse indicates that our results in sample A are consistent with the 400 nm, 400 keV ^{15}N-implanted sample in the study by van Dam *et al.* Further studies are necessary to pin down the source of the repump-triggered variation. Nevertheless, for the ^{15}NV centers, observation of long periods of spectral stability between repumps shows promise for implementation of quantum networks with integrated photonic devices.

Furthermore, we show that this optical stability rapidly degrades with increasing proximity to the diamond surface, corroborating measurements in Ref. [24] of NV centers in thin diamond membranes which showed a strong correlation of reduced NV spectral stability with decreasing membrane thickness, not accompanied by a change in the NV strain environment. Reference [24] suggests that the additional NV dephasing may be attributed to the Ar/Cl$_2$ plasma etch process even for micrometer-scale-thick samples. Our past work has seen a similar effect on implanted centers [14]. Indeed, Ref. [37] shows that $\approx$1 μm thin diamond membranes with improved diamond surface quality (etched by a soft graded O$_2$ plasma) can host NV centers with narrow linewidths.

Our conclusions fit into a larger narrative regarding the source of degradation of other properties near surfaces as well, such as NV T_2. Recent work in Ref. [38] correlating the reduction of NV T_2 within 20 nm of the surface has shown that the T_2 for an NV center within 10 nm of the surface can be enhanced by an order of magnitude by preparing diamonds with smoother surfaces and well-ordered oxygen termination. Further work would need to be done to determine whether the spin bath responsible for T_2 degradation is related to the charge traps we infer in our optical measurements; however, both suggest that solving the surface interaction problem is more important than fixing residual implantation damage.

ACKNOWLEDGMENTS

TABLE I. Plasma processing parameters for preimplantation etch of all diamond samples. ICP, inductively coupled plasma; sccm, cubic centimeters per minute at STP.

Parameter	Ar/Cl$_2$	O$_2$
RF power (W)	240	50
ICP power (W)	320	1500
dc bias (V)	530	150
Chamber pressure (mTorr)	9	25
Ar flow (sccm)	32	0
Cl$_2$ flow (sccm)	20	0
O$_2$ flow (sccm)	0	20
Chuck temperature (°C)	15	15
Total duration (min)	45	20

APPENDIX A: PLASMA PROCESSING DETAILS

We utilize an Oxford Plasmalab-100/ICP-180 etcher. The samples are sandwiched between two sapphire slides held in place with a drop of Crystalbond-509 (applied as a solution in acetone) on a 100 mm sapphire carrier wafer. The total etch duration is broken up into multiple etch cycles involving 5 min of plasma processing followed by a 3 min no-plasma cooldown phase. This ensures that the diamond sample is maintained near the processing temperature. The samples remain in the etcher through the entire two-step process. The etch parameters are provided in Table I.

APPENDIX B: AUTOMATED SPECTROSCOPY PROCEDURE

Confocal scans with off-resonant 532-nm excitation are utilized to generate an NV PL intensity map of the region of interest. First, individual NV centers are identified by image processing (peak prominence detection), and their x, y, and z piezo positions are registered. The linearly polarized excitation is optimized for one set of NV orientations. ODMR, PLE, and low-temperature off-resonant spectra data sets are acquired by iterating through the registered NV centers. During the iteration process, at each registered center the piezo x, y, and z positioners are cycled through three PL optimization sweeps to correct for microscope drift. Before proceeding with pulsed ODMR at RT, a Rabi experiment is manually performed to extract the RF π-pulse specifications for the data set. This is followed by ODMR performed at RT.

Next, the samples are cooled in a closed-cycle 10 K cryostat (Janis CCS-XG-M/204N) for the PLE data set. Because we switch microscopes between automated ODMR (RT) and PLE (LT), the data sets are not correlated. Hence, for our primary correlated data set (samples A and B), consecutive ODMR and PLE measurements were performed manually
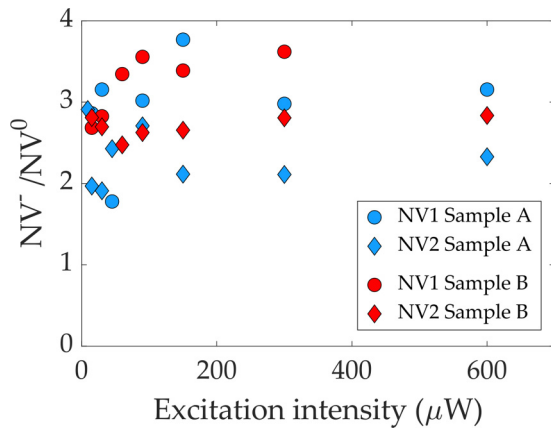
FIG. 6. NV charge state ratio as a function of the 532-nm excitation intensity.

on the same microscope. For each center, PLE is performed in two steps, coarse and fine scans. First, the coarse scans utilize the full range of a New Focus velocity tunable laser ($\approx$85 GHz) to identify the ZPL frequency. Then a set of 30 scans are performed across the identified ZPL (scan range = 5 GHz) with high resolution ($\Delta\nu = 10$ MHz). For samples C, D, and F, a 50 ms off-resonant repump is applied at the end of each scan. For sample E, a repump pulse is only applied if no NV PL is observed during the scan (i.e., indicating that the NV has ionized to the neutral charge state). In postpro-

cessing, each scan is fitted to a Lorentzian, and the average FWHM of the fits is calculated. During analysis, a set of preset criteria (peak intensity, fitted FWHM, and fit shape) are used to discard scans with ionization events. The average FWHM distribution thus computed for all NV centers in the data set is shown in Fig. 4. No sideband or microwave driving was used for the automated PLE data sets.

Finally, off-resonant ZPL spectra are collected for registered NV centers with an 1800 g/mm Princeton Acton 2750 spectrometer ($\Delta\lambda = 0.0208$ nm). Here, if multiple peaks are observed in individual spectra, they are recorded as independent peaks. We do not distinguish the different transitions associated with the NV excited state spin sublevels. To identify the excited state structure with confidence would require a confirmation of a single NV in the excitation spot, obtained via a photon autocorrelation measurement, which is time intensive and not currently feasible with the automated process.

APPENDIX C: NV$^-$-to-NV^0 CHARGE STATE RATIO

To determine the preferred NV charge state, we look at the ratio of NV$^-$ and NV^0 ZPL intensities at $\lambda = 637$ and 575 nm, respectively (Fig. 6). The NV spectra are measured under off-resonant excitation at 12 K. The NV$^-$ charge state is predominant throughout the observed excitation range (NV$^-$/NV^0 typically >2) for implanted NV centers in both samples A and B.

[1] M. W. Doherty, N. B. Manson, P. Delaney, F. Jelezko, J. Wrachtrup, and L. C. Hollenberg, Phys. Rep. **528**, 1 (2013).

[2] F. Jelezko and J. Wrachtrup, Phys. Status Solidi A **203**, 3207 (2006).

[3] L. Robledo, L. Childress, H. Bernien, B. Hensen, P. F. Alkemade, and R. Hanson, Nature (London) **477**, 574 (2011).

[4] M. H. Abobeih, J. Cramer, M. A. Bakker, N. Kalb, M. Markham, D. J. Twitchen, and T. H. Taminiau, Nat. Commun. **9**, 2552 (2018).

[5] H. J. Kimble, Nature (London) **453**, 1023 (2008).

[6] S. Wehner, D. Elkouss, and R. Hanson, Science **362**, eaam9288 (2018).

[7] P. C. Humphreys, N. Kalb, J. P. J. Morits, R. N. Schouten, R. F. L. Vermeulen, D. J. Twitchen, M. Markham, and R. Hanson, Nature (London) **558**, 268 (2018).

[8] M. Pompili, S. L. Hermans, S. Baier, H. K. Beukers, P. C. Humphreys, R. N. Schouten, R. F. Vermeulen, M. J. Tiggelman, L. dos Santos Martins, B. Dirkse, S. Wehner, and R. Hanson, Science **372**, 259 (2021).

[9] C. Bradley, J. Randall, M. Abobeih, R. Berrevoets, M. Degen, M. Bakker, M. Markham, D. Twitchen, and T. Taminiau, Phys. Rev. X **9**, 031045 (2019).

[10] N. Kalb, A. A. Reiserer, P. C. Humphreys, J. J. Bakermans, S. J. Kamerling, N. H. Nickerson, S. C. Benjamin, D. J. Twitchen, M. Markham, and R. Hanson, Science **356**, 928 (2017).

[11] T. Schröder, S. L. Mouradian, J. Zheng, M. E. Trusheim, M. Walsh, E. H. Chen, L. Li, I. Bayn, and D. Englund, J. Opt. Soc. Am. B **33**, B65 (2016).

[12] N. H. Wan, T.-J. Lu, K. C. Chen, M. P. Walsh, M. E. Trusheim, L. De Santis, E. A. Bersin, I. B. Harris, S. L. Mouradian, I. R. Christen, E. S. Bielejec, and D. Englund, Nature (London) **583**, 226 (2020).

[13] M. Gould, E. R. Schmidgall, S. Dadgostar, F. Hatami, and K.-M. C. Fu, Phys. Rev. Appl. **6**, 011001(R) (2016).

[14] S. Chakravarthi, P. Chao, C. Pederson, S. Molesky, A. Ivanov, K. Hestroffer, F. Hatami, A. W. Rodriguez, and K.-M. C. Fu, Optica **7**, 1805 (2020).

[15] E. R. Schmidgall, S. Chakravarthi, M. Gould, I. R. Christen, K. Hestroffer, F. Hatami, and K.-M. C. Fu, Nano Lett. **18**, 1175 (2018).

[16] S. B. van Dam, M. Walsh, M. J. Degen, E. Bersin, S. L. Mouradian, A. Galiullin, M. Ruf, M. IJspeert, T. H. Taminiau, R. Hanson, and D. R. Englund, Phys. Rev. B **99**, 161203(R) (2019).

[17] M. Kasperczyk, J. Zuber, A. Barfuss, J. Kölbl, V. Yurgens, S. Flågan, T. Jakubczyk, B. Shields, R. Warburton, and P. Maletinsky, Phys. Rev. B **102**, 075312 (2020).

[18] C. Santori, P. E. Barclay, K.-M. C. Fu, and R. G. Beausoleil, Phys. Rev. B **79**, 125313 (2009).

[19] G. Davies, S. C. Lawson, A. T. Collins, A. Mainwood, and S. J. Sharp, Phys. Rev. B **46**, 13157 (1992).

[20] S. J. Breuer and P. R. Briddon, Phys. Rev. B **51**, 6984 (1995).

[21] X. J. Hu, Y. B. Dai, R. B. Li, H. S. Shen, and X. C. He, Solid State Commun. **122**, 45 (2002).

[22] V. M. Acosta, C. Santori, A. Faraon, Z. Huang, K.-M. C. Fu, A. Stacey, D. A. Simpson, K. Ganesan, S. Tomljenovic-Hanic,

A. D. Greentree, S. Prawer, and R. G. Beausoleil, Phys. Rev. Lett. **108**, 206401 (2012).

[23] Y. Chu, N. de Leon, B. Shields, B. Hausmann, R. Evans, E. Togan, M. J. Burek, M. Markham, A. Stacey, A. Zibrov, A. Yacoby, D. Twitchen, M. Loncar, H. Park, P. Maletinsky, and M. Lukin, Nano Lett. **14**, 1982 (2014).

[24] M. Ruf, M. IJspeert, S. van Dam, N. de Jong, H. van den Berg, G. Evers, and R. Hanson, Nano Lett. **19**, 3987 (2019).

[25] C. Lee, E. Gu, M. Dawson, I. Friel, and G. Scarsbrook, Diamond Relat. Mater. **17**, 1292 (2008).

[26] J. F. Ziegler, M. D. Ziegler, and J. P. Biersack, Nucl. Instrum. Methods Phys. Res., Sect. B **268**, 1818 (2010).

[27] K.-M. C. Fu, C. Santori, P. E. Barclay, and R. G. Beausoleil, Appl. Phys. Lett. **96**, 121907 (2010).

[28] H. Yamano, S. Kawai, K. Kato, T. Kageura, M. Inaba, T. Okada, I. Higashimata, M. Haruyama, T. Tanii, K. Yamada, S. Onoda, W. Kada, O. Hanaizumi, T. Teraji, J. Isoya, and H. Kawarada, Jpn. J. Appl. Phys. **56**, 04CK08 (2017).

[29] M. L. Goldman, M. W. Doherty, A. Sipahigil, N. Y. Yao, S. D. Bennett, N. B. Manson, A. Kubanek, and M. D. Lukin, Phys. Rev. B **91**, 165201 (2015).

[30] J.-P. Tetienne, L. Rondin, P. Spinicelli, M. Chipaux, T. Debuisschert, J.-F. Roch, and V. Jacques, New J. Phys. **14**, 103033 (2012).

[31] T. Yamamoto, S. Onoda, T. Ohshima, T. Teraji, K. Watanabe, S. Koizumi, T. Umeda, L. P. McGuinness, C. Müller, B. Naydenov, F. Dolde, H. Fedder, J. Honert, M. L. Markham, D. J.

Twitchen, J. Wrachtrup, F. Jelezko, and J. Isoya, Phys. Rev. B **90**, 081117(R) (2014).

[32] C. Santori, P. Tamarat, P. Neumann, J. Wrachtrup, D. Fattal, R. G. Beausoleil, J. Rabeau, P. Olivero, A. D. Greentree, S. Prawer, F. Jelezko, and P. Hemmer, Phys. Rev. Lett. **97**, 247401 (2006).

[33] P. Tamarat, N. B. Manson, J. P. Harrison, R. L. McMurtrie, A. Nizovtsev, C. Santori, R. G. Beausoleil, P. Neumann, T. Gaebel, F. Jelezko, P. Hemmer, and J. Wrachtrup, New J. Phys. **10**, 045004 (2008).

[34] K.-M. C. Fu, C. Santori, P. E. Barclay, L. J. Rogers, N. B. Manson, and R. G. Beausoleil, Phys. Rev. Lett. **103**, 256404 (2009).

[35] A. M. Edmonds, U. F. S. D'Haenens-Johansson, R. J. Cruddace, M. E. Newton, K.-M. C. Fu, C. Santori, R. G. Beausoleil, D. J. Twitchen, and M. L. Markham, Phys. Rev. B **86**, 035201 (2012).

[36] P. Siyushev, H. Pinto, M. Vörös, A. Gali, F. Jelezko, and J. Wrachtrup, Phys. Rev. Lett. **110**, 167402 (2013).

[37] I. Lekavicius, T. Oo, and H. Wang, J. Appl. Phys. (Melville, NY) **126**, 214301 (2019).

[38] S. Sangtawesin, B. L. Dwyer, S. Srinivasan, J. J. Allred, L. V. Rodgers, K. De Greve, A. Stacey, N. Dontschuk, K. M. O'Donnell, D. Hu, D. A. Evans, C. Jaye, D. A. Fischer, M. L. Markham, D. J. Twitchen, H. Park, M. D. Lukin, and N. P. de Leon, Phys. Rev. X **9**, 031052 (2019).